Available online at www.sciencedirect.com
ScienceDirect
Ultramicroscopy 108 (2008) 179–195
ultramicroscopy
www.elsevier.com/locate/ultramic

An electron microscope for the aberration-corrected era

O.L. Krivanek*, G.J. Corbin, N. Dellby, B.F. Elston, R.J. Keyse, M.F. Murfitt, C.S. Own, Z.S. Szilagyi, J.W. Woodruff

Nion Co., 1102 8th Street, Kirkland, WA 98033, USA

Abstract

Improved resolution made possible by aberration correction has greatly increased the demands on the performance of all parts of high-end electron microscopes. In order to meet these demands, we have designed and built an entirely new scanning transmission electron microscope (STEM). The microscope includes a flexible illumination system that allows the properties of its probe to be changed on-the-fly, a third-generation aberration corrector which corrects all geometric aberrations up to fifth order, an ultra-responsive yet stable five-axis sample stage, and a flexible configuration of optimized detectors. The microscope features many innovations, such as a modular column assembled from building blocks that can be stacked in almost any order, *in situ* storage and cleaning facilities for up to five samples, computer-controlled loading of samples into the column, and self-diagnosing electronics. The microscope construction is described, and examples of its capabilities are shown.

PACS: 07.78.+s; 42.15.Fr; 41.85.−p; 68.37.Hk; 06.60.Sx

Keywords: Aberration correction; STEM design; Sample stage; HAADF imaging; EELS

1. Introduction

Correction of electron-optical aberrations is a field with a 60-year history [1,2], which has blossomed in the last 10 years. Aberration correctors have significantly improved the performance of scanning electron microscopes (SEMs) [3], transmission electron microscopes (TEMs) [4] and scanning transmission electron microscopes (STEMs) [5–7]. Aberration-corrected electron microscopes are now finding their way into mainstream usage in large numbers. The attainable STEM resolution has improved by about 2.5 ×, and the current available in a given-size small probe has increased by about 10 ×. Further major improvements are expected when a new generation of instruments such as the one described here come fully on-line.

The microscope column itself, on the other hand, has not improved to a similar extent. The electron guns, round lenses, objective lens (OL) polepieces, sample stages, and detectors available in present-day instruments are quite similar to the best available 20–30 years ago. This is exemplified by the Topcon 002B, introduced in 1986, which featured double-winding round lenses able to maintain constant heat output even as their magnetic excitation was changed, a condenser-OL with spherical aberration coefficient $C_s = 0.4$ mm and chromatic aberration coefficient $C_c = 0.8$ mm (at 200 kV), an illumination system consisting of five lenses, toroidal deflectors with minimized hysteresis, and a reasonably stable side-entry sample stage [8,9]. It was a well-rounded instrument, optimized for 2 Å resolution, which was the norm for the top instruments of its day. Even the best non-aberration corrected dedicated STEM, the 300 kV VG HB603 [10], did not manage to improve on many of these characteristics.

The lack of progress in microscope design is surprising in view of the fact that aberration-corrected instruments are now approaching 0.5 Å resolution, and that atomic-resolution elemental mapping by electron energy-loss spectroscopy (EELS) and energy-dispersive X-ray spectroscopy (EDXS), which place serious demands on long-term

*Corresponding author.
E-mail address: krivanek.ondrej@gmail.com (O.L. Krivanek).

0304-3991/$ - see front matter © 2007 Elsevier B.V. All rights reserved.
doi:10.1016/j.ultramic.2007.07.010

stability, are about to become established techniques. The continued use of aging design elements has resulted in a situation whereby today's highest-performance microscopes are so sensitive that the designers of the microscopes' foundations need to be concerned about the pounding of ocean waves on a shore 30 miles distant [11]. The microscopes need to be housed in custom-built labs with special vibration-free foundations, thorough sound shielding, minimized stray magnetic fields, and air temperature that is kept constant to within 0.1 °C [11,12]. Even with these precautions, they remain sensitive to adventitious disturbances such as pressure changes due to doors opening and closing, and the low frequency magnetic fields due to passing trucks [12].

At Nion, we have decided to adopt a different approach: design an entirely new instrument in a way that takes the increased demands into account right from the start. Other fundamental goals of the design were to give the instrument as much flexibility as possible, and at the same time to automate its basic operation so that even novice microscopists can use the instrument near its full potential. One more very important goal was to make the microscope completely computer-controlled, so that its full functionality, including sample exchange, would be available to remote users over the Internet.

2. Design overview

The new microscope has been developed on two parallel but converging paths. Its electron-optical column was designed, built, and tested using a 100 kV VG cold field emission gun (CFEG) as the electron source, and is now fully functional. At the same time, a 200 kV CFEG is being developed separately. This gun is now fully built up, but it is still being tested. It will be the subject of a separate publication.

Fig. 1a shows the new column, and Fig. 1b shows its schematic cross-section. The VG 100 kV gun has a very good vacuum (typically in the low 10^{-11} Torr range), stability such that the emission current from a freshly cleaned tip takes 40 min or more to decay to 50%, brightness $>10^{13}$ A/(m^2 sr) at 100 kV, and energy spread ~0.3 eV. We have used the basic gun plus its high-voltage tank, but replaced the control electronics with a digital design that is computer-controlled, and water-cooled for improved stability.

Electron-optically, the new column starts with a pair of deflectors for steering the beam coming up from the gun, and continues with three round condenser lenses, a quadrupole–octupole C_3/C_5 corrector, a quadrupole triplet called quadrupole lens module (QLM) for coupling the corrector electron-optically to the OL, a lower OL winding module, sample stage/OL polepiece module, an upper OL winding module, four round projector lenses, and a detector column that includes several detectors and other devices: a high-angle annular dark-field (HAADF) detector, a pneumatically controlled beam stop that can be inserted when recording diffraction patterns, medium angle annular dark-field (MAADF) detector, bright field (BF) detector, a quadrupole/octupole module called quadrupole–octupole coupling module (QOCM) for optimized coupling of inelastically scattered electrons into an electron energy loss spectrometer, a 1k × 1k fast read-out CCD camera for Ronchigram, diffraction pattern and image read out, an EELS entrance aperture and finally an electron energy-loss spectrometer, typically a Gatan Enfina.

The column has been designed for 200 kV operation. Operation at 100 kV and lower voltages is possible and actually involves several advantages, such as reduced knock-on damage in light element materials. When the column is interfaced to the VG 100 kV CFEG, it outperforms the aberration-corrected version of the VG column (VG condensers, OL and sample stage, plus Nion C_s corrector) in essentially all respects.

The column is entirely modular. All the modules are 275 mm in diameter and either 60 mm or a multiple of 60 mm in height. They all have the same mechanical interface, and can therefore be stacked in practically any order.

Each module of the Nion column has integral double μ-metal magnetic shielding. Measured sensitivity to stray magnetic fields at 100 kV is 0.6 Å r.m.s. probe movement per 1 mG r.m.s. of uniform 60-cycle fields. Measurement of sensitivity to localized AC fields showed the shielding to be the weakest at the top of the VG gun. We expect that with Nion's own CFEG, the sensitivity will be reduced further.

In addition to the lens and detector modules listed above, there are also three pumping/aperture modules. These modules provide several different functions, as needed at their particular locations: a vacuum connection to a pump, a pneumatically controlled gate valve, an aperture that can be shifted mechanically and electrically, an electrostatic beam blanker, and an in-column μ-metal shield that decouples the magnetic excitation of lenses above and below the shield. The modules have the standard mechanical interface, and can be placed anywhere in the column.

In the present design, the first pumping/aperture module is placed between the first and second condenser lenses. It contains a vacuum connection to the condensers' ion pump, a pneumatic gate valve that can isolate the gun from the rest of the microscope, an aperture and a beam blanker. A second pumping module is placed between the upper OL winding and the first projector lens. It contains a vacuum connection to the projectors' ion pump and a magnetic shield that eliminates small magnetic cross-talk that would otherwise occur between the projectors and the OL. A third pumping module is placed between the last projector lens and the detectors. It provides a vacuum connection to the detectors' ion pump and a pneumatic gate valve that can isolate the detectors from the rest of the microscope, for operations such as changing a scintillator or servicing the EELS.

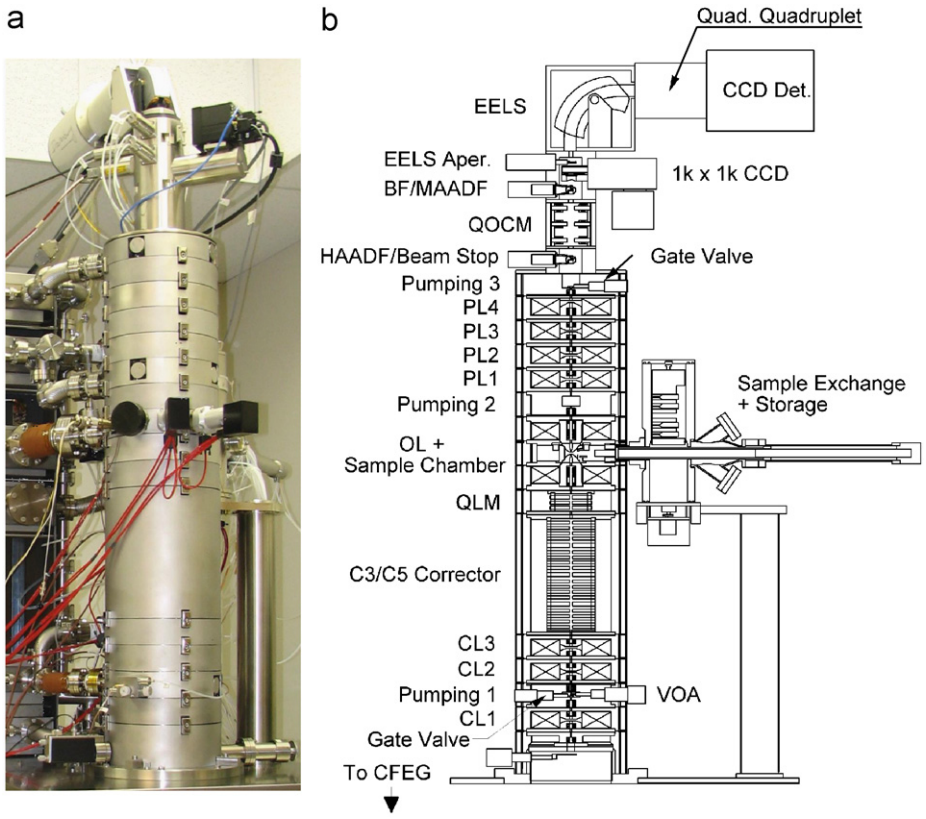

Fig. 1. (a) The new column and (b) schematic cross-section of the column.

The modularity of the column means that different configurations can be adopted quickly and easily. For instance, we first assembled the microscope with only two condenser and two projector lenses, but changed this to three condensers and four projectors for greater flexibility in adjusting the angular range and current of the probe, and in forming diffraction patterns and CTEM images. Further lenses and other modules can be added later, even after installation. Equally importantly, the sample stage module, which follows the same modular scheme, can be removed and replaced by another one and the microscope can be back in operation typically in less than one day.

2.1. Round lenses

Each one of the column's round condenser and projector lenses contains an interchangeable polepiece which allows its minimum focal length (f_{min}) to be chosen as needed. To suit the different requirements placed on each particular lens, we presently use three types of polepieces: a symmetric polepiece with $f_{min} = 15$ mm, a smaller-gap symmetric polepiece with $f_{min} = 4$ mm, and an asymmetric polepiece with $f_{min} = 4$ mm. To obtain the best possible tolerances on the alignment of the top and bottom polepieces, we machine them in the same way that OL polepieces are made for most other microscopes: the polepieces are first joined together by a non-magnetic spacer, and the final machining is carried out only on the joined assembly.

Each lens also contains two magnetic deflectors, which ensure that the incoming beam is sent into the lens along the lens axis, and is then passed onto the next optical stage as needed by that stage. This gives the whole column the same alignment flexibility as if each lens had mechanical "shifts" (shifting the lens sideways) and "tilts" (shifting one polepiece mechanically w.r.t. the other), but without the inconvenience and tendency to drift inherent to mechanical shifters. Because of the good alignment of the upper and lower polepieces attained by machining them together, the optical axis of the lens is typically found to coincide with the mechanical axis of the whole column to better than 0.5°. This means that the magnetic fields needed to reach proper alignment are quite weak, and the deflectors do not make a major contribution to the overall stability budget for the whole microscope.

All the round lenses have double windings, wound in an interleaved fashion. The lenses are supplied by two independent power supplies such that the power dissipation is held constant at all the different magnetic excitation settings. This means that changing the lens setting does not change its heat output, and does not result in thermal drift that could otherwise affect the microscope stability for tens of minutes after the change. Because the OL has a lower and an upper winding, each one of which is double-wound,

the OL uses a total of four windings and is powered by four separate current supplies. The total cross-section of its lens coils has made the total power dissipated in the OL less than 150 W at 100 kV.

The three condensers used in our standard column allow the illumination angle to be varied widely, from <1 mrad semi-angle to >40 mrad. The beam current can be adjusted at the same time by changing the demagnification of the field-emission source. The whole adjustment range is available using just a single virtual objective aperture (VOA), typically of 30 μm diameter. Fig. 2 shows how this is done. The gun lens (C0) is typically run at constant excitation such that it produces a crossover near the gun's differential pumping aperture (but it could be used to shift all regimes towards higher or lower probe currents). C_1 then becomes the lens that sets the probe current. When it produces a crossover far from the VOA, smaller beam current and larger source demagnification (i.e., better resolution but noisier data) result. This is shown in Fig. 2a. When the crossover produced by C_1 moves closer to the VOA (Fig. 2b), a larger beam current, less source demagnification, and bigger probes result. C_2 is then adjusted to give the same beam diameter in C_3 as for the higher demagnification mode, and C_3 is adjusted to produce the same beam divergence (typically a parallel beam). For the two modes, the beam arriving at the corrector then appears to originate from the same place in the column. It also has the same diameter (and hence the same convergence angle at the sample), but different source demagnifications.

In practice, several different source demagnification modes are made available to the user, to make it possible to select the right probe current to suit the application at hand. The switching between the modes is accomplished in a few seconds, and the probe generally moves by less than 10 nm relative to its previous location. Because C_1 to C_3 are all run in the constant-power mode, no long-term drift results from the switchover.

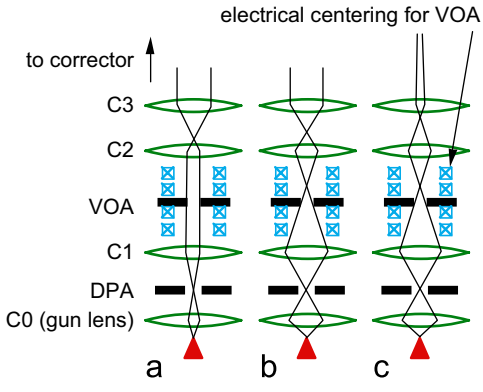

Fig. 2. Different probe setup regimes made possible by the three condensers: (a) small, convergent probe with large source demagnification, (b) small convergent probe with less source demagnification (and hence bigger probe current) and (c) larger but more parallel probe with the same beam current as (b). Note that the virtual objective aperture remains the same for all the regimes.

To decrease the convergence angle of the probe illuminating the sample, as for instance needed for parallel-beam diffraction and TEM imaging, the diameter of the beam sent up to the corrector needs to be decreased. This is done by adjusting C_2 so that the crossover it produces is shifted closer to C_3, and adjusting C_3 so that the beam coming out of it is again nearly parallel. This is shown in Fig. 2c. Leaving C_1 unchanged leaves the beam current the same as for the more convergent probe setup (cf. Fig. 2b), and of course C_1 can also be changed to adjust the beam current as needed.

The OL is a symmetric, Riecke-Ruska type [13] condenser-OL. Our standard high-resolution polepiece has a gap of 4 mm and a bore of 1.5 mm, and is therefore better optimized for low chromatic aberration (C_c, which we do not correct in this column), than for spherical aberration (C_s, which we do correct). Its focal length is $f=1.5$ mm for both the pre-field and post-field parts, its calculated aberration coefficients are $C_s=1.1$ mm, $C_c=0.95$ mm at 100 kV, and $C_s=1.0$ mm, $C_c=1.1$ mm at 200 kV. The polepiece is a part of the sample stage module, and is therefore changed whenever the sample chamber is switched with another one.

The four projectors give a wide range of camera lengths for diffraction pattern recording, from <10 mm to >1 m on the main CCD camera. The diffraction patterns are properly focused, i.e. the pattern appearing on the CCD does not shift or grow fuzzy when the probe is scanning over a large sample area. The four projectors also allow conventional TEM (CTEM) imaging (which is not aberration corrected in our standard column, whose main emphasis is on STEM), at magnifications of up to 400,000 ×. Even without the addition of further round lenses (which is easy to do with our column), both the camera length and the magnification ranges can be extended further by the use of the pre-CCD QOCM.

Just like in a regular CTEM, high-magnification CTEM imaging in the Nion column requires the first projector (P1) to run near its maximum strength, and the OL to project a focused image of the sample into the front-focal plane of P1. The OL excitation and sample height used for CTEM imaging turn out to be close to the optimum setup for the formation of distortion-free diffraction patterns extending up to the maximum angles allowed by the OL's upper bore, and could therefore be used as the starting point for diffraction modes and for coupling into the EELS. However, the maximum angle that can be collected on the HAADF detector can be increased by about 20% if the post-sample part of the OL is underfocused slightly so that the real image of the sample produced by the OL moves beyond P1. This means that the sample needs to be raised by a small amount (about 5 μm) and the OL excitation slightly weakened. This constitutes our standard mode of setting up the projector lenses for STEM signal detection.

In this standard regime, P1 is weakly excited so that it focuses on the diffraction pattern in the back-focal plane of the OL. The regime amounts to coupling into the

projectors with an angular compression factor of about 150 due to the OL alone. Under the typical STEM detection setup (see Section 2.3), the projectors reduce this compression to about 10 × for the beam leaving P4, and also allow the compression (i.e., the camera length of the diffraction pattern) to be varied while the diffraction pattern stays in focus.

A critical consideration when the projector column is run in this way is that even small changes in the sample height, of the order of a few μm, change the regime considerably. It is therefore important that the sample height inside the OL be controlled with precision better than about 100 nm.This is accomplished very competently by the (X, Y, Z, α, β) five-axis stage described in Section 2.4.

The column can also be run with the OL excitation set to zero. This makes the probe about 100 × less convergent than when the OL is on, and thus about 100 × larger. The available camera lengths also increase by about 100 ×. BF and DF images can nevertheless still be formed. The mode is very useful for low magnification "survey" imaging, at fields of view up to about 1 mm, and it may also be useful for studying long-range order by very high-resolution diffraction, at camera lengths of 10 m and more. Because the OL coils are double-wound, the magnetic field of the lens is turned off without any change in its overall heating, thus eliminating long-term drift that would have resulted with a single-winding OL.

2.2. Aberration corrector

The aberration corrector is our third-generation design. It has been described in detail previously [14–16]. It uses 12 rotatable quadrupoles and three combined quadrupole–octupoles. The three quadrupole–octupoles correct third-order axial aberrations, similar to our second-generation design [5,6]. Unlike in the previous design, in the new design the quadrupole–octupoles are precisely imaged into each other, and the third quadrupole–octupole is imaged into the coma-free plane of the OL. The magnification is different in different transverse directions. There is a round beam in the first quadrupole–octupole, an elliptical beam elongated in one transverse direction in the second one, and an elliptical beam elongated in the perpendicular direction in the third one.

The optical conditions described above allow third-order axial aberrations to be corrected without introducing combination fifth-order axial aberrations. A quadrupole quadruplet (4 quadrupoles) is needed for imaging each quadrupole–octupole into the next, a quadrupole triplet is used to couple the beam arriving from the condensers into the bottom quadrupole–octupole, and finally a quadrupole quadruplet is used to couple the third quadrupole–octupole into the OL. One of the final quadrupoles is a part of the corrector; three more are located in the QLM placed between the corrector and the OL.

The corrector is 30 cm long and therefore amounts to a quintuple-height module. Its magnetic polepieces are made and aligned to each other with better than 10 μm precision. The axial trajectories through the corrector are shown in Fig. 3a. By combining octupoles with quadrupoles, we are able to operate in a regime in which the beam is relatively narrow everywhere except in the quadrupole–octupoles themselves. This is precisely the general arrangement that minimizes the contribution of the corrector to the overall chromatic aberration budget [16]. In our particular case, the C_c contribution of the corrector amounts to 0.21 mm.

Fig. 3b shows the field trajectories. They demonstrate how the corrector's quadrupole–octupoles are imaged into each other, and the last quadrupole–octupole is imaged into the coma-free plane of the OL. In reality, this last imaging is slightly misadjusted. The resultant combination C_5 [15,16] is used to null the C_5 inherent to the optical system, i.e. to correct the principal fifth-order spherical aberration. This is what allows the corrector to null fifth order aberrations in addition to the third-order aberrations.

Each quadrupole layer of the corrector needs four current supplies: one each for its "normal" and "skew" quadrupoles, plus one each for its X and Y dipoles. The quadrupole–octupole layers need five supplies. The corrector therefore uses a total of 48 + 15 = 63 power supplies. A further 12 supplies are used in the QLM just above the corrector, meaning that 75 high-stability current supplies are required by this part of the column.

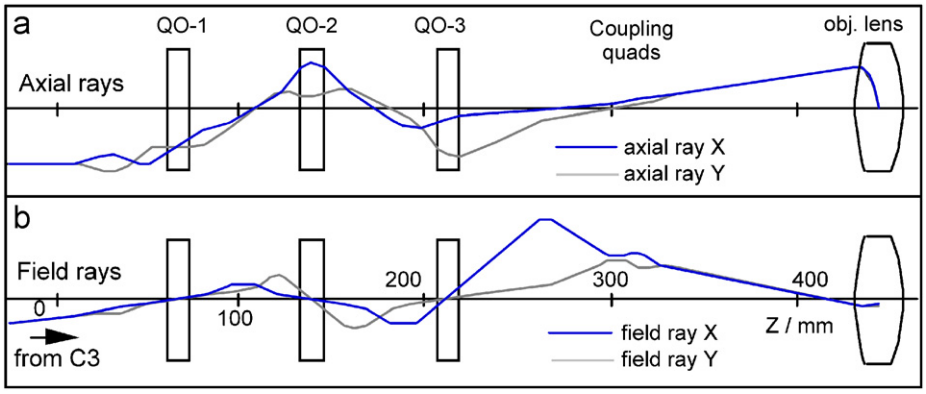

Fig. 3. Axial (a) and field (b) trajectories through the C_3/C_5 corrector.

The large number of elements and power supplies has given the corrector a large number of degrees of freedom, both for using different types of trajectories to attain the desired correction, and even more so for the different ways the corrector can be misaligned. At the same time, the precision with which the corrector needs to be set up has gone up considerably compared to C_3-only correctors. This has resulted in a new paradigm, in which the human operator is no longer able to manually bring up the corrector trajectories or perform a subsequent full re-alignment, both of which could still be done by an experienced operator using our second-generation corrector.

To overcome this limitation, we have developed software that analyzes the beam trajectory through the corrector layer-by-layer, and iteratively brings it in into agreement with the desired trajectories predicted by the computer. The software automatically compensates for linear sample drift during the measurement. It requires between 5 and 30 min per iteration, depending on how close or far to the desired solution the corrector is. 10–15 iterations are typically required during the initial bringup procedure to set all the aberration coefficients, including fourth- and fifth-order ones, to be smaller than the desired limits. Fortunately, the resultant setup is found to be quite stable, and the full initial alignment procedure does not need to be repeated except if the corrector has been disassembled and put back together again.

The day-to-day ''touch-up'' alignment typically only needs to tune aberrations of third and lower orders, and is performed in a few minutes.

2.3. Detectors

The detector system is designed to give a large degree of flexibility and automation. It is able to detect several signals simultaneously, and to select which signals will be detected purely under software control. A cross-section through the detector system is shown in Fig. 4.

Just like the main column, the detector part of the microscope column is modular. However, the detector modules are only 120 mm in diameter. This brings the photomultiplier tubes (PMTs) closer to the scintillators, helping to optimize their coupling efficiency. In the standard configuration of the system, there are two separate annular STEM detectors that use a scintillator coupled to a PMT.

STEM detector I is located in front of the quadrupole–octupole coupling module (QOCM), the STEM detector II after the QOCM. The column section above the QOCM also houses the 1k × 1k CCD camera and further an EELS entrance aperture.

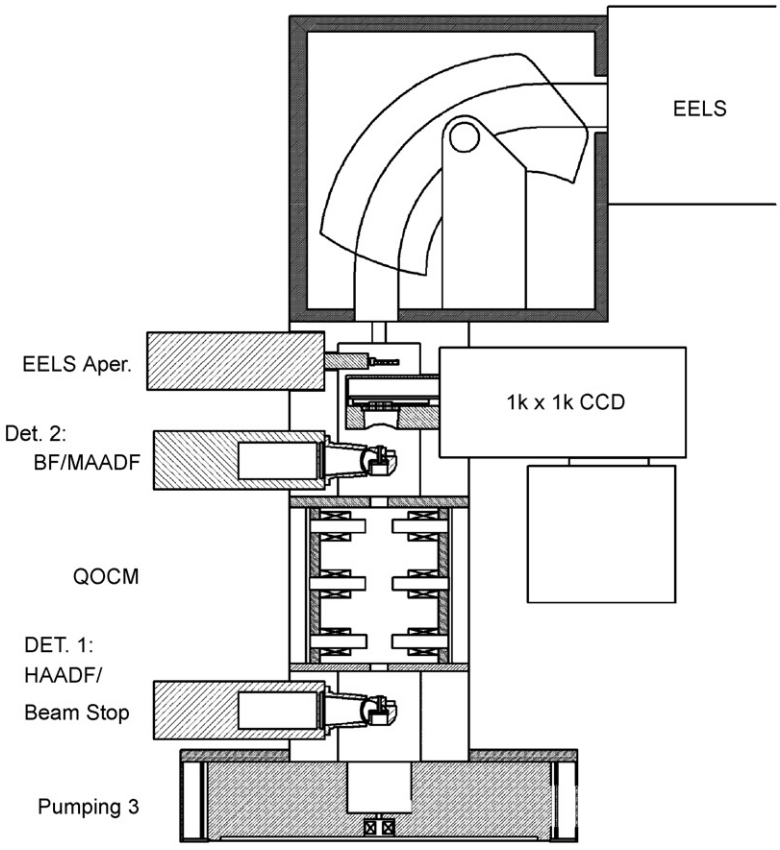

Fig. 4. Schematic cross-section through the detector section of the column. The scintillators of the HAADF detector/beam stop and the BF/MAADF detectors, the CCD camera, and the EELS aperture can all be inserted/removed into/from their on-axis positions using pneumatic mechanisms.

Detector I has three working positions: (i) high-angle annular dark-field (HAADF) detector; (ii) beam-stop for obscuring the (0, 0) spot in quasi-parallel-beam diffraction patterns; and (iii) both the HAADF and the beam stop removed, for unobstructed recording of Ronchigrams and diffraction patterns by the CCD.

Detector II also has three working positions: (i) medium-angle annular dark-field (MAADF) detector, (ii) bright field (BF) detector, (iii) both detectors removed from the beam for unobstructed Ronchigram and diffraction pattern recording by the CCD.

The scintillator part of the STEM detectors uses interchangeable modules that include the scintillator, a scintillator liner consisting of a thin metallic tube that shields the non-conductive scintillator hole, and a parabolic mirror that reflects the generated photons towards the PMT. The modules are fastened into a scintillator carrier capable of holding two such modules, and are moved pneumatically into an on-axis position that faces the PMT. A fine mechanical adjustment is provided for centering the scintillators on the detector module's axis. The scintillators themselves are made of single-crystal YAP. About 2000 photons are generated by each incident electron, and about 100 of the photons reach the cathode of the PMT. This allows for very efficient signal detection. It also means that single electron counting could be readily implemented for very weak signals such as those used in low-dose biological work.

The CCD camera is mounted just above STEM detector II. It uses a $1k \times 1k$ CCD chip with a separate read-out area and a 15 MHz read-out rate. The whole image detected by the CCD is first shifted into the read-out area, and then read out. The shift is performed in less than 1 ms, and no beam shuttering is therefore required. Up to 15 full-size images can be recorded and displayed per second, or up to 30 images that are binned to 512×512. At the same time, recording times of a few seconds can be used for time integration of weak features. The chip uses anti-blooming technology, which is useful when recording spot diffraction patterns. The pixel size is $14 \times 14\,\mu m^2$, and the chip is fiber-optically coupled to a P32 powder scintillator. The camera moves in-and-out using a bellows seal and pneumatic activation. The CCD chip and other temperature-sensitive camera components can be removed from the column without breaking the vacuum, which needs to be done when baking the whole microscope.

Above the CCD, there is a 4-position EELS entrance aperture, also pneumatically controlled, and finally an electron energy-loss spectrometer. The Gatan Enfina, which is able to record spectra at a fast rate with good DQE and a wide range of dispersion values, and has extensive software for spectrum analysis and spectrum-imaging, is used.

The optics of the Enfina has some known limitations: it lacks an electrical adjustment for one of the three important second-order spectrum aberrations, and it has no third-order aberration adjustments. This is not a serious limitation for normal TEM EELS performed at around 1 eV energy resolution with a typical 2 mm entrance aperture. However, with a CFER, energy resolution better than 0.4 eV is readily achievable, and the resolution loss due to the spectrometer should be minimized, ideally to <0.1 eV. At the same time, entrance beams of 2–3 mm diameter are needed to avoid having to "compress" the angular distribution excessively, as this would result in too much sensitivity to probe movement, and it could also lead to the C_s of the OL post-sample field affecting the spectrum resolution in a major way.

In the Nion microscope, these limitations are overcome by the QOCM. This module uses three quadrupole–octupoles to perform the following functions:

(a) Adjust the height of the entrance crossover seen by the spectrometer. This has the effect of changing the second-order spectrum aberration that is not electrically adjustable by the Enfina itself. Together with the trim coils for the other two second-order aberrations provided by the Enfina, the system is therefore able to tune all the second order spectrum aberrations.
(b) Provide electrical adjustments for all four third-order spectrum aberrations.
(c) Provide an extra lens for modifying the camera length of the diffraction patterns or the magnification of the images to be recorded by the CCD camera. This lens has the advantage that it allows the camera length of the diffraction pattern at the CCD to be varied relative to the camera length on the HAADF detector. This makes it possible to expand the inner cone admitted by the HAADF scintillator so that it covers nearly the whole CCD, which is useful for higher-resolution viewing of Ronchigrams. It also allows the camera length on the BF detector to be changed relative to the HAADF detector, which is useful when recording HAADF and BF images simultaneously.

Typical operating modes of the detector setup are shown in Table 1. The gaps between shown ranges are typically due to scintillator liners. Other collection angle combinations can be obtained by adjusting the round projector lenses, the QOCM, or by replacing the modular scintillators by ones with different diameters.

2.4. Sample stage

The sample stage is a fundamentally new design. It employs radial symmetry in such a manner that when the temperature of the whole stage changes uniformly, there is no change in the sample position, to first order. This is illustrated in Fig. 5, which shows that the balls that drive the stage push against surfaces that are parallel to thermal expansion directions. Provided that the sample cartridge and the cartridge housing are made from the same material as the stage ring, thermal expansion therefore results in no shift of the sample relative to the microscope axis.

Table 1
Different detection modes of the microscope

Detector name	Mode name					
	HAADF +EELS	HAADF +MAADF +EELS	HAAD +BF	HAAD +CCD (Ronchi-gram)	CCD (diffraction pattern)	CCD (TEM image)
HAADF (det. I)	80–240	80–240	80–240	80–240	–	–
MAADF (det. II)	–	40–60	–		–	–
BF (alt. det. II)	–	–	<40[a]		–	–
CCD	–	–	–	0–60	10 mm $\leqslant$ CL $\leqslant$ 1 m[b]	100 × $\leqslant$ mag $\leqslant$ 400k ×[c]
EELS	0–60	0–30	–			
Illum. apert. (α)	$\leqslant$50	$\leqslant$30	$\leqslant$50	Any		

The table lists the half-angles (in mrad) intercepted by each particular detector. The angular radius of the illumination aperture appropriate to each mode is also shown.

[a]Defined by an aperture placed in front of the BF detector and the QOCM setup. Typically about 3 mrad.

[b]10 mm CL corresponds to a 100 mrad half-angle falling 1 mm from the center of the CCD (and therefore being usable by the EELS, which typically operates with a 2.5 mm diameter entrance aperture). 1 m CL corresponds to $\pm$7 mrad field of view on the CCD.

[c]OL is off for mag $<$ 3k ×. The top magnification can be extended to $>$1M × by using the QOCM in addition to the projectors.

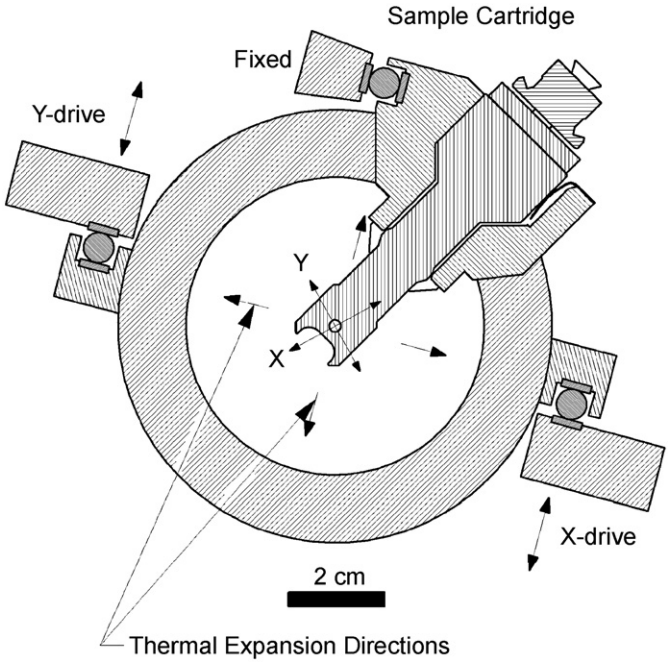

Fig. 5. Schematic illustration showing that uniform thermal expansion of the stage has no first-order effect on the position of the sample.

In contrast, side-entry stages are very sensitive to changes in temperature, as anyone who has used a side-entry stage of a microscope sited in a room with poor temperature regulation can attest.

A major design aim for the stage was to eliminate friction, dead travel and backlash as much as possible. Accordingly, the X, Y and Z stage drives only do a total of four motion transfers each, from one moving part onto the next, in order to couple the rotation of their stepper motors to the motion of the sample. The drives employ only elastic hinges and pre-loaded ball bearings to achieve nearly zero-friction motion with no backlash or hysteresis. This is all different from traditional stage drive designs, which typically do many more motion transfers (e.g., the X-drive of the Topcon 002B does seven transfers), several of which are not backlash-free.

A potential weakness of friction-free designs like ours is that without friction, energy of vibrations does not readily dissipate, which could make the stage vibration-prone. We have overcome this by providing the stage with adjustable vibration dampers, and by making the stage lightweight and stiff. (Higher resonant frequencies make it harder for vibrations to couple into the stage efficiently, and make them dissipate faster.) The result is that the lowest measured resonant frequency of the stage is 950 Hz. With the dampers properly adjusted, the stage "glides" into a new position on a time scale of about 0.5 s, and has good mechanical stability even in a fairly noisy acoustic environment.

As described in Section 2.8, stepper motors for the X, Y and Z drives have about 3.5 million addressable steps covering the motion range. The range is $\pm$1.5 mm (for X and Y) and $\pm$1 mm (for Z). This means that if the stage were completely friction-free, the steppers would allow smallest motion steps of about 1 nm in all three directions. Working with the stage shows that the smallest actual X and Y steps are about 2 nm. This means that we were rather successful in eliminating mechanical friction, but not completely so. The sample height Z can be changed with about 5 nm precision and the Z-motion causes less than 20 nm of sideways (X, Y) motion (for defocus changes $<1\,\mu$m). The sample can therefore be brought close to correct focus mechanically, which has the great advantage that the pre-sample and post-sample optical conditions remain unchanged.

The double-tilt cartridge designed for the stage features a new mechanism with two tilt axes that are at 90° to each

other and 45° to the principal cartridge axis. It achieves ±30° tilt in any direction (in a 4 mm polepiece gap). The same stepper motor mechanisms are used for the tilts as for the *X*, *Y*, *Z* drives, and have a total number of addressable motor positions of about 3 million for the ±30° tilt range. The cartridge uses miniature ball bearings for friction-free operation, but the motion coupling is less direct and less friction-free than for the *X*, *Y*, *Z* drives. The result is that the cartridge has demonstrated reproducible tilt steps of about 0.5 mrad (0.03°). This corresponds to an atom at the top of a 1000 Å thick sample moving sideways by 0.5 Å w.r.t. an atom at the bottom of the sample, and should be more than adequate for nearly all microscopy needs.

A 5-axis stage (*X*, *Y*, *Z*, *α*, *β*) with the above degree of mechanical precision can be readily computerized to provide eucentric tilting along two axes [17]. The appropriate software is being developed and tested. One of the capabilities of the software will be "point-and-click tilting": while looking at a live image of a diffraction pattern, the user will be able to click on a location in the pattern, whereupon the sample will be tilted so that the direction corresponding to the clicked location becomes parallel with the beam direction. This will mean that when the center of a zero-order Laue zone visible in a single-crystal diffraction pattern is clicked on, the corresponding zone axis will become aligned with the microscope beam axis. The software will also automatically compensate for any changes in *X*, *Y*, *Z* positions that will result from tilting the sample, and the user will be presented with a new diffraction pattern from the same area, at the same height in the polepiece, but with the new tilt.

2.5. Sample storage/airlock

Up to five sample cartridges can be loaded into the microscope at the same time, evacuated, and then inserted into the in-column (observation) position under computer

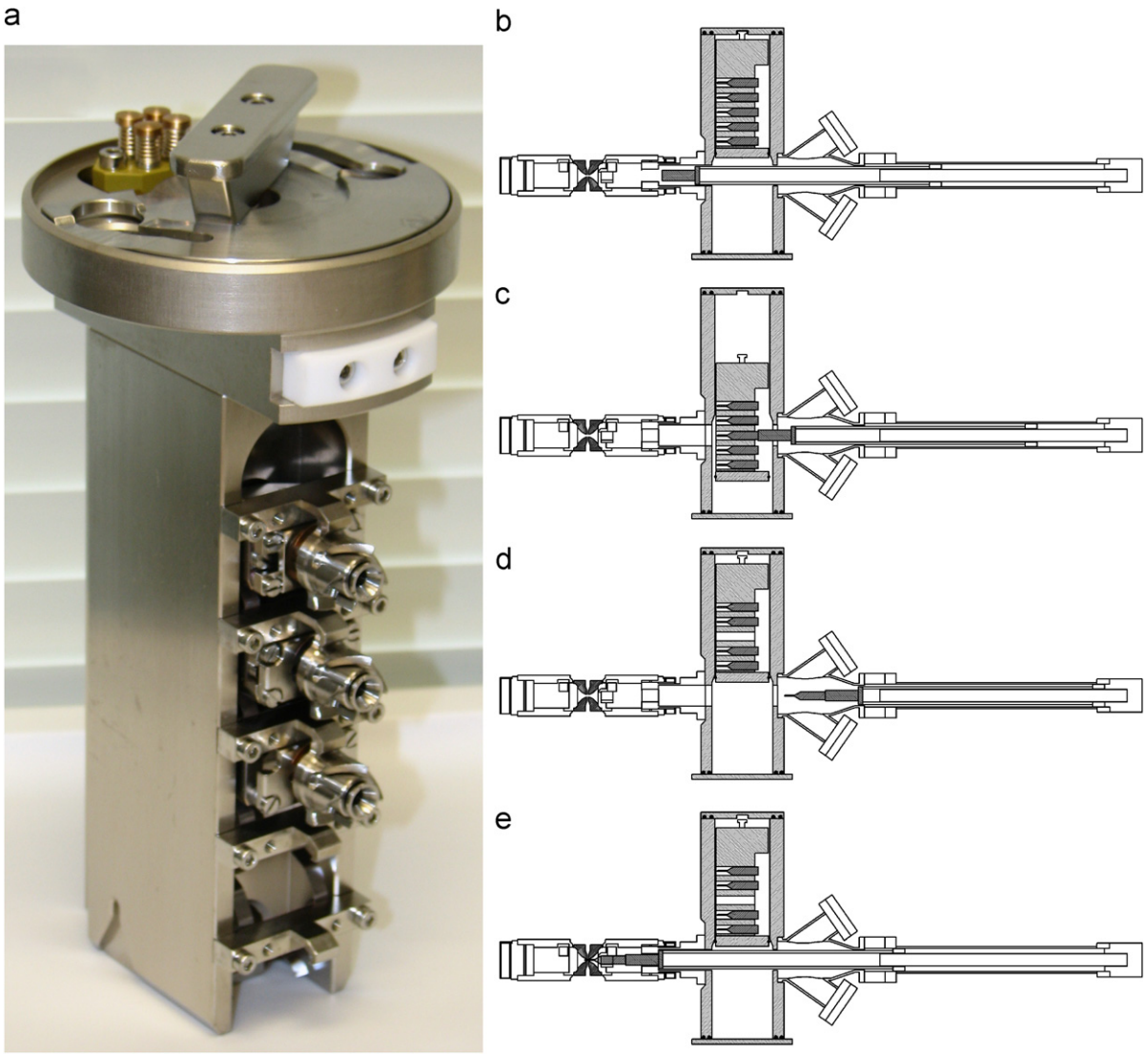

Fig. 6. (a) The storage magazine, loaded up with three sample cartridges. (b)–(e) Schematic diagrams of the sample storage and loading mechanism.

control. The magazine that holds the cartridges and the different working positions of the storage/loading mechanism are shown in Fig. 6.

The magazine (Fig. 6a) is normally stored in a "storage chamber", which is attached to the side of the microscope column. The upper part of the chamber serves as an airlock. It is isolated from the rest of the storage chamber whenever the receptacle for the cartridge magazine is in its topmost position (Fig. 6b). The magazine is inserted into the airlock manually, the lid (which has two Viton O-rings, differentially pumped) is closed, and the rest of the evacuation/insertion sequence is performed under computer control. The first part of the evacuation is done by a turbo pre-pumping station, with the magazine in the topmost position. While the newly inserted magazine is still in the airlock and being pumped by the turbo, it can be baked at 120–140 °C, also under computer control. It is then lowered into the storage chamber proper, where the pumping is provided by a 30 l/s ion pump. From there, sample cartridges are individually selected (Fig. 6c) and moved into the sample stage by a pneumatically driven arm (Fig. 6e). While the magazine is moved up and down, the exchange arm (with or without a sample on it) is fully retracted into a "preparation chamber" to stay free of the magazine (Fig. 6d). Two ports are provided on the preparation chamber for optional ion guns (or other attachments) with a line-of-sight towards the sample, for sample cleaning and/or thinning.

The system allows a magazine with five cartridges to be inserted into the microscope and evacuated, and the samples to be cleaned by heating or other means. The user can then select any one of the five samples for observation, under computer control. Five samples should typically be enough for an experimental session. While the session is proceeding, a second magazine can be prepared with its complement of samples. The magazines can then be swapped, and the next user can start operating the microscope in less time than if all the previous samples had to be offloaded first from their cartridges to make room for new samples.

2.6. Scanning and data acquisition system

The Nion scan/magnification/acquisition system is designed to drive four layers of scan coils, as required for complete freedom in scanning and descanning the probe, vary the magnification as required, and digitize several signals simultaneously.

The scanning of the beam is performed by four fast deflectors (lower X, lower Y, upper X, upper Y) in the lower bore of the OL, plus four deflectors in the upper bore of the lens. The result is that arbitrary scan/descan operations, such as those needed for wide area EELS mapping or for confocal STEM [18] can be performed. Another ability inherent to the design is rock/derock, as needed for conical precession recording of spot diffraction patterns [19] and for EELS ALCHEMI [20]. We expect these abilities to lead to a blossoming of the techniques that require these types of scans.

The electronics driving the scan coils are shown schematically in Fig. 7. The basic addressable scan field is $64k \times 64k$ in size. Software driving the scan circuits can perform expected operations such as sub-area scan and scan rotation. The minimum per-pixel dwell time is 167 ns, meaning that up to six $1k \times 1k$ scanned images can be acquired per second (and twenty four 512×512 ones). At this fast rate, the circuitry can digitize two signals simultaneously, at 16 bits each. At slightly slower rates, up to four signals can be digitized in the "standard" configuration, and up to twelve signals total if extra digitization boards (and detectors) are added.

The scanning system can also be driven by an external scan generator, which then provides analog ramps to drive the X and Y scans, and digitizes the amplified signals from the PMTs (and other detector devices) supplied to it by the Nion electronics. The Nion Scan/Magnification/Acquisition system is then used to produce the correctly scaled currents that need to go to the four layers of scan and descan coils. This includes the magnification function, i.e. the scan currents sent to the different coils are scaled as appropriate for the desired magnification. The internal/external scan switchover is controlled by software. It provides the Nion microscope with an ability to use special software written only for specific scan generators, such as the Gatan spectrum-imaging software, which presently requires the DigiScan (or DigiScan II) to run.

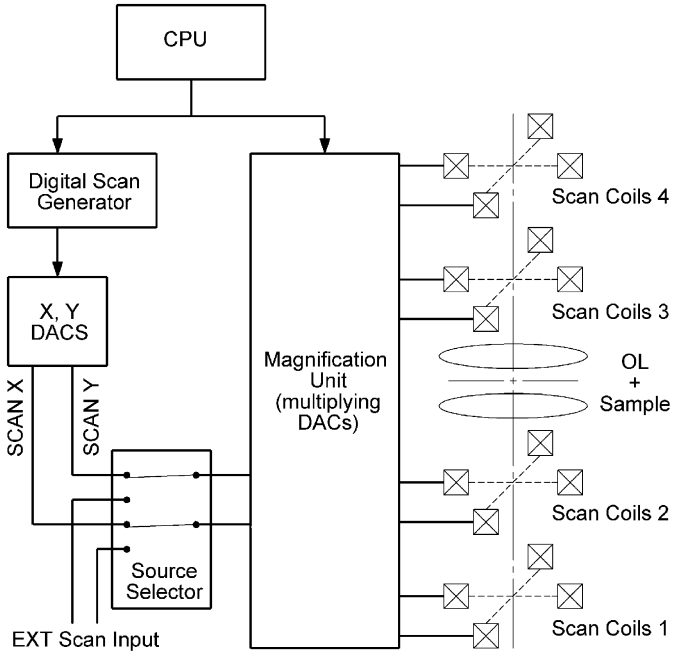

Fig. 7. Schematic diagram of the scan and magnification parts of the scan/magnification/acquisition unit.

2.7. Vacuum system

The whole vacuum system is entirely dry—no diffusion or rotary oil pumps are used. Pumping of the airlock and pre-pumping of the microscope is done by a 70 l/s turbomolecular pump backed by a dry scroll pump. The rest of the pumping is done by ion pumps. The entire system is computer-controlled, including all the pumps and pneumatically operated valves.

The microscope is divided into eight separate vacuum sections: (1) the gun, (2) the gun/column "interface", (3) condensers plus corrector, (4) sample stage/OL, (5) projectors, (6) detectors, (7) sample storage chamber and (8) roughing/guard vacuum. The first five sections (the main column from the gun to the projectors) use only metal seals and are pumped by ion pumps, one pump for each section. Relatively small pumps (20 or 30 l/s capacity) are used, but because the pumped volumes are small and contain no O-rings sealing against atmosphere, the vacuum levels in these sections are typically in the 10^{-9} Torr range. The gun/column interface section normally stays in the 10^{-10} Torr range. This minimizes the streaming of gases from the column into the gun, which is important for stable CFEG operation.

The large number of vacuum sections provides excellent vacuum separation between the gun and the rest of the column. For example, even a sample chamber pressure of 1×10^{-6} Torr has no measurable effect on the gun vacuum (when in the 10^{-11} Torr range), and a detector pressure in the 10^{-6} Torr range has no measurable effect on the sample chamber vacuum (when in the 10^{-9} Torr range).

The column modules are coupled vacuum-wise using miniature copper gaskets. These are proving very reliable: so far, we have had only one column gasket that failed to seal on initial assembly, and no vacuum leaks at all from a previously vacuum-tight gasket.

The sample storage chamber uses double Viton seals with guard (differential) vacuum, and operates typically in the 10^{-8} Torr range (but worse right after a change of the cartridge magazine). In the detector section, single Viton O-rings are used, and the vacuum level is typically around 3×10^{-7} Torr. This is entirely tolerable: the vacuum isolation of the detectors from the rest of the column is very good, making the exact vacuum level at the detectors unimportant.

The whole column is bakeable to 140 °C. This includes all the round lenses, the corrector, the sample stage and the pumping modules. We find in practice that 120 °C bakes are equally effective in eliminating oils that cause contamination, and therefore typically bake at this temperature. After a bake, the column vacuum tends to keep on improving, as is typical of metal-seal-only systems, rather than get worse, as is typical of systems sealed with O-rings.

2.8. Electronics

The microscope electronics fit in three standard instrumentation racks that house 48 cm (19 in) wide electronic modules. Each rack is 180 cm tall. They are called Vacuum Rack, Power Rack and Instrumentation Rack, respectively. Their functions are indicated by their names: one controls the vacuum system, one provides the raw power for the rest of the electronics, and one provides a noise-free environment for housing the high-stability current supplies that control the instrument's electron optics.

The high-stability supplies come in two major types: ultra-high stability, low-power current supplies that provide the currents needed to drive the dipoles, quadrupoles and octupoles of the column, and higher power, high-stability current supplies that drive the round lenses. The low-power supplies provide about 0.03 ppm short- and long-term stability. The high-power supply boards are housed in identical backplane chassis units and provide better than 0.1 ppm stability.

In addition to the current supply boards, there are three other types of boards that are housed in the standard backplane chassis: stepper motor control boards, precision stepper motor control boards, and HT power supply boards for PMTs and beam blankers.

The stepper motor control is designed for controlling high-power, high-speed stepper motors such as the one that moves the cartridge storage magazine up and down. The precision stepper motor control is designed for slightly slower but more precise stepping. It provides 384 micro-steps per step, and it can handle up to three motors per board. There are two such boards per microscope; one is used for the X, Y and Z stage stepper motors, and one for α and β tilt drive steppers. The stepper motors have 400 steps per revolution, which means that there are 153 600 micro-steps per each revolution of the stepper, and about 3.5 million individually selectable micro-steps available over the entire range of motion of each separate stage control.

The PMT power supply board can provide supply voltages adjustable from 0 to 1000 V for up to four photomultiplier tubes. The voltages applied to the PMT dynodes are individually regulated, and do not change when the PMT current changes. This eliminates a major source of nonlinearities in PMT detectors. Another possible source of nonlinearities, an adjustable dark level that has been misadjusted such that signal clipping is occurring [21], has also been eliminated, simply by not providing any adjustable analog offset for the PMT signal. Yet another possible source of nonlinearities (or cross-talk between signals), namely fast-changing unipolar signals produced by the detector that radiate from the cables and can also couple into the ground, has been eliminated by using paired-output signal amplifiers which send an analog signal plus its anti-signal down a twisted pair cable that goes from the microscope to the digitizing unit.

There is also a fifth HT supply on each one of the PMT supply boards, which provides 300 V for driving the beam-blanker circuit. The circuit itself is housed away from the board, closer to the microscope column, for faster beam-blanker response.

Just like the column, the electronics are also entirely modular. A new column section is accommodated by adding the appropriate power supply boards into available slots in any one of the backplane chassis units, or by adding another chassis, if required.

Because the power supply settings do not need to be changed very frequently, the computer communicates with the power supply boards via an RS-232 serial interface. The communication is bidirectional: the computer requests the boards to supply the desired output currents to the various coils the boards are hooked up to, and the boards measure the actual output signal, and report back to the computer what the measured values are. In this way, it is easy to diagnose a malfunctioning board or a bad connection to a coil in the column. This level of cross-checking was found to be essential in view of the large number of power supplies involved.

Much faster communication is needed for the Scan/Magnification/Acquisition unit. We use USB2, which has a maximum throughput rate of 480 Mbits per second, for this purpose.

2.9. Software

The control software is also modular. It runs on two personal computers (PCs) under Windows XP: a ''Hardware'' computer and a ''User'' computer.

The Hardware computer, as its name implies, handles all the hardware, with the exception of data acquisition devices, which need high data transfer rates. It communicates with the precision current supplies, the high-voltage electronics, and the vacuum system: it sets them to the values needed, and handles the communication whereby they send back information on their actual states. It also communicates with the User computer, informing it about the state of the hardware, and receiving commands as to what to do next.

None of these tasks places high demands on the Hardware computer, which means that this computer does not need to be particularly fast.

The User computer runs processing-intensive software modules, and therefore needs to be a high-end PC. It also handles high-speed data acquisition, and provides high-level control of the microscope's lenses and other physical devices. The software that runs on it includes all the modules that the regular user is expected to interact with:

- AutoSTEM2, which provides the user with an interface for controlling the electron optics of the column at a high level. AutoSTEM2 is able to create and modify ''compound'' controls, which adjust several optical elements at the same time, in the precise proportions required to produce ''pure'' effects. It does this by communicating with software modules running on the Hardware computer that control the actual power supplies and are called DACWIN1, DACWIN2, etc.
- SuperScan, which controls the Nion Scan/Magnification/Acquisition unit, setting up the various scans as needed and receiving the digitized data.
- CCDCam, which handles the acquisition of the Ronchigrams, diffraction patterns and TEM images by the Nion 1k × 1k CCD camera.
- Gatan's DigitalMicrograph, which handles data acquisition and processing of EELS data from the Gatan Enfina spectrometer.
- Enfina CCD controller, which reads out the spectra recorded by the Enfina's CCD.
- FilterControl, which sets the currents (and one voltage) in the optical elements of the Enfina.

DigitalMicrograph is a high-level software module that provides advanced functions such as image analysis and processing, EEL Spectrum analysis, EEL Spectrum-Imaging, automated tuning of the spectrometer, etc.

Both Nion AutoSTEM2 and Gatan DigitalMicrograph provide advanced scripting languages, as well as an ability to run compiled plug-in modules. These capabilities are used by many of the more sophisticated routines of the Nion software, such as routines that perform automatic aberration diagnosis, and routines that analyze and fine-tune the electron-optical trajectories through the corrector.

3. Expected performance

3.1. Overall performance

There are many operating modes that the new microscope is expected to be able to perform, such as STEM and CTEM imaging, convergent and parallel beam diffraction, and EELS analysis. Most of the modes have been described in the preceding sections that covered the individual components of the column. The descriptions make it clear that the new microscope was designed to be very flexible already in its standard configuration.

The microscope offers even more flexibility if its electron-optical elements are re-arranged to suit new requirements. For instance, for biological low-dose STEM imaging at about 2 Å HAADF resolution, the condenser-side corrector is not needed. The column can be readily assembled without the corrector, resulting in a compact STEM that retains many of the features described above. Another interesting permutation would be to add a projector-side corrector. As a by-product of managing the electron trajectories so that fifth-order aberrations are corrected, the C_3/C_5 corrector has a wide field of view [22]. It could be readily used as a CTEM corrector too, providing much improved CTEM imaging.

3.2. Probe size and current

The probe size and the beam current in a STEM are principally determined by four factors: geometric aberrations, chromatic aberrations, the source brightness, and

instabilities. The resolution attained in an image is determined by the probe size and current, and by the beam–sample interaction.

The geometric aberrations of the probe-forming optics define the size of the aberration-free "sweet spot" [6] in the illumination aperture plane. For a C_5-corrected system in which the first-, third- and fifth-order aberrations are set up to optimally oppose uncorrected seventh-order geometric aberrations and in which parasitic aberrations up to sixth order are nulled with sufficient precision, the maximum usable illumination angle (i.e. the radius of the sweet spot) is given by

$$\alpha_{\mathrm{geom}} = (50\lambda/(|C_{7,0}| + 2|C_{7,2}| + 6|C_{7,4}| + 18|C_{7,6}| + 50|C_{7,8}|))^{1/8}, \quad (1)$$

where λ is the electron wavelength and the different multipliers take into account how well the different seventh-order aberrations can be compensated by lower order ones.

The calculated values for $C_{7,0}$, $C_{7,2}$, $C_{7,4}$, $C_{7,6}$ and $C_{7,8}$ of the new corrector are 8.2, 1.8, 9.2, 2.5 and 1.2 cm respectively. The corresponding α_{geom} values are 57 mrad at 100 kV and 54 mrad at 200 kV.

The size of the sweet spot that an ASTEM can attain gives a limit on the size of the largest usable illumination aperture. This then gives a diffraction limit on the attainable resolution when imaging with an illumination cone of half-angle α:

$$d_{\mathrm{geom}} = 0.61\,\lambda/\alpha_{\mathrm{geom}}, \quad (2)$$

where d_{geom} is the full-width at half-maximum (FWHM) of the resultant probe due to geometric aberrations. The sweet spots of 57 and 54 mrad given above result in d_{geom} of 0.40 Å at 100 kV, and 0.28 Å at 200 kV.

The effect of chromatic aberration also depends on α, but in a more subtle way. In HAADF imaging, partial beams passing near the edges of the illumination aperture are equally distant from the optic axis. This is the condition for their interference not to be influenced by chromatic effects, which only affect interference between beams passing at different distances from the optic axis. Interference between beams passing near the edges of the aperture is what gives rise to the highest spatial frequencies present in the image. Paradoxically, this means that a significant portion of high spatial frequencies contributing to a HAADF image remains even when chromatic effects are important. However, a high percentage of lower spatial frequencies, which arise by interference of partial beams that are at different distances from the optic axis, is lost due to the same chromatic effects. Overall this means that in the presence of significant chromatic effects (e.g. a sizeable energy spread of the beam) the probe tends to exhibit a sharp central peak, surrounded by an extended "tail".

This effect is modeled most simply by working out the fraction of the intensity that remains in the central peak of the probe when chromatic aberration is diverting some intensity into the probe tail. This "fraction remaining" is given by [15]:

$$f_{\mathrm{r}} \sim 1 - (1 - w)^2, \quad (3)$$

where $w = 0.75\lambda E_0/(\Delta E\, C_{\mathrm{c}}\, \alpha^2)$ or $w = 1$, whichever is smaller. C_{c} is the coefficient of chromatic aberration of the probe-forming optics, E_0 the primary energy, α is once more the half-angle of illumination, and ΔE the full-width at half-maximum of the probe's energy distribution that is due to the CFEG energy spread plus high-voltage instabilities. (Contributions to chromatic aberration due to variations of the OL current, which are typically <0.1 ppm, can be neglected in our system.)

Selecting a larger value of α decreases f_{r}, but improves the attainable resolution, up to a limit set by the noise from the tail wiping out the smaller details being imaged by the sharp probe peak. The optimum value of f_{r} depends on the experiment to be performed. For elemental mapping by EELS or EDXS, f_{r} should be >0.9. For HAADF imaging in which capturing the highest spatial frequency detail possible is the main goal, $f_{\mathrm{r}} = 0.5$ is probably still acceptable. Choosing $f_{\mathrm{r}} = 0.75$ as a reasonable middle ground requires that $w = 0.5$ and gives

$$\alpha_{\mathrm{chrom}} = 1.2(\lambda E_0/(\Delta E C_{\mathrm{c}}))^{0.5} \quad (4)$$

and hence

$$d_{\mathrm{chrom}} = 0.5(\lambda C_{\mathrm{c}} \Delta E/E_0)^{0.5}, \quad (5)$$

where d_{chrom} is the resolution limit due to chromatic aberration.

In our column, the OL contributes 1 mm, the condensers 0.1 mm (when run in the high source demagnification mode) and the corrector 0.2 mm towards the probe's chromatic aberration coefficient. For the resultant $C_{\mathrm{c}} = 1.3$ mm and further $\Delta E = 0.35$ V (as appropriate for a W CFEG emitting 5 μA total current), Eq. (5) gives $d_{\mathrm{chrom}} = 0.65$ Å at 100 kV, and $d_{\mathrm{chrom}} = 0.38$ Å at 200 kV, for illumination half-angles of 35 and 40 mrad, respectively.

Since both the geometric and chromatic aberrations lead to a limit on the size of the largest usable illumination aperture and thus to diffraction-limited imaging, the resolution limit is largely set by whichever aberration limits the aperture size more. The above analysis then shows that at 100 kV, the chromatic aberration will be a much more severe limit in our system, and that even at 200 kV, chromatic aberration will be more limiting than geometric aberrations.

This means that in the present system, the geometric aberrations are improved to such an extent that they no longer matter, and other effects have become more limiting. This is not altogether surprising. If chromatic aberration could be neglected, then our new ASTEM would allow imaging with a sweet spot that is $>5\times$ larger in radius and $>25\times$ larger in area than the largest sweet spot of the corresponding uncorrected system.

Further improvements in resolution will require either a more monochromatic beam, still higher primary voltage, or chromatic aberration correction. Options number two and three involve significant disadvantages, whereas the first option brings a major additional advantage: improved energy-resolution EELS. It is the option we plan to explore in the future.

The next important influence on the overall probe size is d_{source}, the size of the demagnified source projected onto the sample. d_{source} depends on the size of the virtual source that represents the field emission tip (typically about 3 nm in a 100 kV CFEG) and on the demagnification setting of the pre-sample optical elements such as condenser lenses. It is independent of the probe size d_{aberr} due to geometric and chromatic aberrations, and the two quantities need to be combined incoherently. A suitable way to do this is to add them up in quadrature, giving:

$$d_{total} = (d_{aberr}^2 + d_{source}^2)^{0.5}. \quad (6)$$

For a reasonable probe current at 100 kV, d_{source} should be of the order of 0.5 Å (see below), giving an expected probe size of ~0.85 Å.

The probe current is given by the source brightness B, the demagnified source size d_{source}, and the illumination half-angle α as

$$I = B\pi^2 d_{source}^2 \alpha^2/4. \quad (7)$$

For $B = 1.5 \times 10^{13}$ A/(m^2 sr) (appropriate for a well-designed CFEG at 100 kV), $d_{source} = 0.5$ Å, and $\alpha = 25$ mrad (as is used in the experimental section below), the above expression gives $I = 60$ pA. To increase the current to 0.5 nA at the same illumination angle, d_{source} has to be increased to 1.5 Å. However, because the chromatic broadening of the probe size only goes up linearly with the illumination angle, the angle can then be opened up to 40 mrad with no further loss of resolution, provided of course that the geometric aberrations are sufficiently well controlled. Setting up the illumination system in such manner will give more than 1 nA of current in a probe about 2 Å in size. This means that when aiming for the highest possible current in a 2 Å probe at 100 kV, the full extent of the aberration-free sweet spot we can regularly reach (see next section) will be usable, giving an additional improvement in the probe current by more than a factor of two.

It also needs to be noted that at 1 Å and bigger probe sizes, one can make the simple approximation that the potential well around the atomic nucleus that is imaged by HAADF is much smaller than the probe, and that HAADF images of isolated heavy atoms lying on a light substrate therefore faithfully reveal the probe shape and intensity. However, for lighter atoms, the potential well around the atomic nucleus is up to a few tenths of an Å wide, and the thermal motion of atomic nuclei at room temperature is around 0.1 Å r.m.s. [23]. As probe sizes become smaller than 1 Å, these blurring effects need to be taken into account when determining the resolution in an image, even for HAADF imaging of isolated atoms. In our particular case it means that the 0.85 Å probe size predicted above should lead to HAADF images whose resolution is just better than 1 Å at 100 kV. This prediction does not take any account of the effects of instabilities, but in our experience, these are typically eventually brought under a sufficient degree of control.

4. Practical performance

4.1. Optics flexibility

The design aims of flexible condenser and projector optics have been largely met. Fig. 8 shows a pair of diffraction patterns acquired from the same area of [1 1 0]-oriented Si. For the first pattern (Fig. 8a), the probe was set up in a convergent mode, as required for STEM imaging. This gave a Ronchigram showing complicated interference patterns between the unscattered beam and the many diffracted beams. Note that even though the central disk spans a diameter of 50 mrad, the fringes seen in the pattern

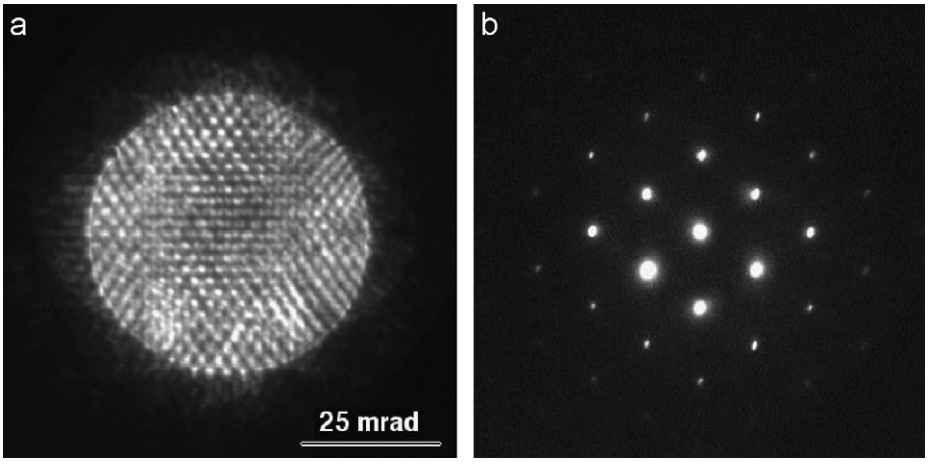

Fig. 8. (a) Convergent beam, out-of-focus diffraction pattern (= Ronchigram) of [1 1 0] Si, and (b) parallel-beam diffraction pattern of the same area. The camera length for both patterns was the same.

run straight. This shows that the aberrations were corrected to a sufficient extent for aberration-free STEM imaging with a probe of this angular range.

The second pattern was recorded immediately after the first one, with the incident beam much more parallel, spanning an angular range of only about 0.5 mrad. The OL and the projector lenses were run exactly as before, i.e. the camera length was not changed. The probe location was also similar. STEM images could also be obtained in this mode, but only at a resolution of about 4 nm. This is nevertheless useful for identifying precipitates, whose structure can then be studied using their point diffraction patterns.

The acquisition time for the diffraction patterns, acquired by the 1k × 1k CCD, was 0.067 s each (15 frames per second). This means that each pattern was integrated over 3.3 cycles of AC mains. The fact that fringes running in all directions, including fringes corresponding to (004)-type interference (1.36 Å), can be clearly distinguished in Fig. 8a means that there were no overwhelming instability issues, including instabilities at AC mains frequencies.

Because the projector column is sufficiently flexible to produce regular CTEM images, the two probe types described above can be directly imaged on the CCD camera. With parallel-beam illumination, phase contrast CTEM resolution was found to be as expected for a 100 kV column with a C_s of 1.1 mm: about 0.3 nm.

4.2. Probe size and current, HAADF and EELS resolution

Fig. 9 shows an experimental Ronchigram obtained with the new microscope, in which the "sweet spot" (the part of the aperture plane that is not affected by geometric aberrations) has a radius of 40 mrad. The theoretical prediction that takes into account seventh-order aberrations that limit the performance of the new corrector is actually 57 mrad half-angle at 100 kV (see Section 3.2). However, this theoretical size does not include any contributions from parasitic aberrations or from instabilities. A less optimistic sweet spot of 50 mrad is also indicated in the figure (as a dashed circle), together with sweet spots reachable by Nion's previous C_3-only corrector, and by an uncorrected 100 kV STEM.

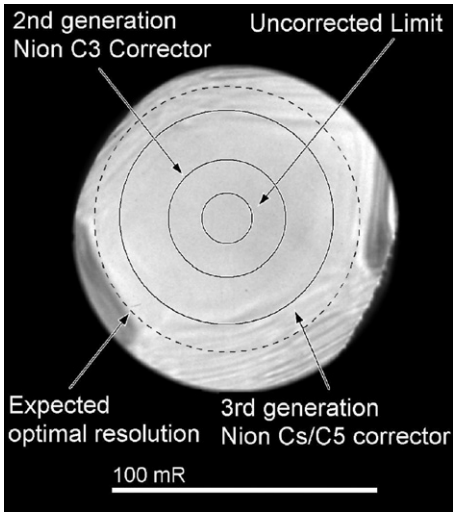

Fig. 9. An experimental Ronchigram obtained with the C_3/C_5 corrector that is a part of the present column, demonstrating correction up to 40 mrad half-angle. The best sweet spot theoretically obtainable with the new corrector, the sweet spot obtainable with Nion's previous (C_3-only) corrector, and the sweet spot of the microscope running with the corrector turned off are also indicated.

Limited precision of tuning is the most likely reason why we have not reached sweet spots greater than 40 mrad yet. The precision of autotuning algorithms improves as the resolution improves, in an iterative manner. As explained in Section 3.2, however, chromatic aberration prevents us from improving the resolution much past 1 Å at 100 kV, and this limits the precision of the tuning. At 200 kV, chromatic aberration will be less of a limit, and the precision of the tuning is expected to improve correspondingly.

Fig. 10 shows a HAADF image and an electron energy-loss spectrum of $SrTiO_3$ recorded at 100 kV with the new microscope. The illumination half-angle was 40 mr, the beam current was 320 pA and the HAADF image (Fig. 10a) per-pixel dwell time was 5 μs. At this acquisition speed, the non-line-synched 512 × 512 pixel image was recorded in 1.3 s. Even so, an FFT of the image (inset) shows that spacings of 1.23 and 0.97 Å were captured.

The microscope's post-sample coupling optics collected angles up to about 50 mr half-angle into the Gatan Enfina parallel EELS. Fig. 10b shows a background-subtracted energy loss spectrum of the Ti $L_{2,3}$ edge threshold peak, collected in 0.5 s with 0.2 eV/channel dispersion. The usual 4-fold splitting is clearly resolved, and the signal-to-noise ratio is excellent for the short acquisition time used.

Similar resolution images and EELS spectra have been recorded at beam currents of up to 0.7 nA with the new microscope. A beam current of this magnitude gives signal-to-noise ratios in EELS data that allow elemental mapping to be carried out at dwell times of the order of a few ms per-pixel, i.e. less than a minute for a 64 × 64 pixel elemental map [24]. The probe diameter is 1–1.5 Å even at these currents. This set of experimental parameters is likely to lead to atomic-resolution, two-dimensional chemical maps, first for elements with especially favorable EELS edges (e.g., first and second transition row metals plus rare earths and actinides) and later on for virtually all elements as the technique improves further. The maps will be accompanied by an ability to probe the bonding and electronic structure, also with atomic resolution. This combination of techniques promises to become a major enabling tool of nanotechnology.

5. Conclusion

A new aberration-corrected STEM column has been designed and is now operational. It incorporates many new

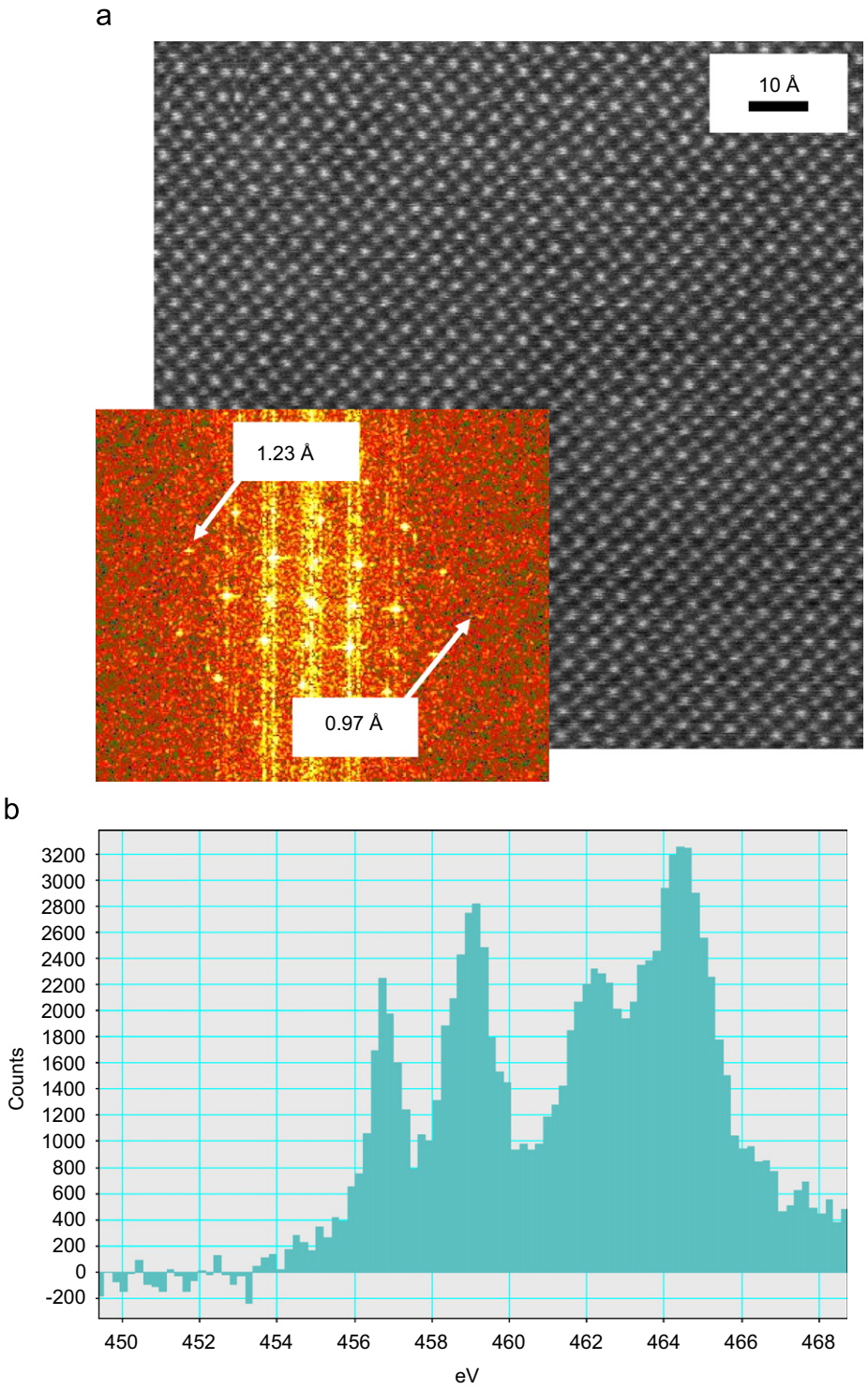

Fig. 10. (a) HAADF image of $SrTiO_3$. 100 keV, 320 pA probe current, 512 × 512 pixels, 5 μs dwell time per pixel. The FFT (inset) shows that spacing of 1.23 and 0.97 Å were resolved. (b) Background-subtracted electron energy-loss spectrum of the Ti $L_{2,3}$ edge. Nion coupling optics, Gatan Enfina parallel-detection spectrometer, acquisition time 0.5 s.

features that make it well suited for the high performance made possible by aberration correction, as described above.

The construction of the column gives it probe-forming and data-collecting capabilities that are essentially only limited by the characteristics of its CFEG. The flexibility of the column gives it many new operating modes, previously available only to those using custom modifications that were typically home-built. Should an application nevertheless arise that the microscope is not

ready for, the modularity of the column and of the electronics will almost certainly allow the microscope to be reconfigured for the new mode, even after it was built.

The first two columns of the type described here have been recently installed in their respective laboratories (spring and autumn 2007). Similar to the way our second-generation correctors produced many revolutionary results once users started working with them, we expect the new instruments to quickly prove their abilities, and to go on to exciting new applications nobody has yet fully imagined.

Acknowledgment

We are greatly indebted to our collaborators, especially to Drs. P.E. Batson, A.L. Bleloch, and S.J. Pennycook, and to Profs. L.M. Brown, C. Colliex and J. Silcox, for giving us the opportunity and challenge to build the new microscope, and for their many specific inputs. Partial funding from NSF (grant number DMR-9977547) and in kind-contributions from Gatan Inc. and Sandia National Laboratory are gratefully acknowledged. Further sincere thanks are due to Dr. A.L. Bleloch for his help in obtaining the results shown in Fig. 8 and to Prof. D.A. Muller and L. Fitting Kourkoutis for the results shown in Fig. 10.

References

[1] O. Scherzer, Optik 2 (1947) 114.
[2] P.W. Hawkes, E. Kasper, Principles of Electron Optics, vol. 2, Academic Press, New York, 1996, pp. 857–863.
[3] J. Zach, M. Haider, Optik 99 (1995) 112.
[4] M. Haider, et al., J. Electron Microscopy 47 (1998) 395.
[5] O.L. Krivanek, N. Dellby, A.R. Lupini, Ultramicroscopy 78 (1999) 1.
[6] N. Dellby, et al., J. Electron Microscopy 50 (2001) 177.
[7] P.E. Batson, N. Dellby, O.L. Krivanek, Nature 418 (2002) 617.
[8] T. Yanaka, Proceedings of the 11th International EM Congress, vol. 1, Japanese Society for Electron Microscopy, Kyoto, 1986, p. 243.
[9] O.L. Krivanek, in: P.R. Buseck, J.M. Cowley, L. Eyring (Eds.), High-Resolution Transmission Electron Microscopy, Oxford, 1988, p. 519.
[10] H.S. von Harrach, Microsc. Microstr. Microanal. 5 (1994) 153.
[11] M.A. O'Keefe, et al., Ultramicroscopy 89 (2001) 215.
[12] D.A. Muller, et al., Ultramicroscopy 106 (2006) 1033.
[13] W.D. Riecke, in: P.W. Hawkes (Ed.), Magnetic Electron Lenses, Springer, Berlin, 1982, p. 163.
[14] O.L. Krivanek, N. Dellby, P.D. Nellist, US patent #6,770,887.
[15] O.L. Krivanek, et al., Ultramicroscopy 96 (2003) 229.
[16] N. Dellby, O.L. Krivanek, M.F. Murfitt, CPO-7 Proceedings, 2006, p. 79, available at: 〈http://www.mebs.co.uk/Abstract%20Book.pdf〉.
[17] C.S. Own et al., Proceedings of Microscopy and Microanalysis, Chicago 1105CD, 2006.
[18] N. Zaluzec, Microscopy Today 6 (2003) 8.
[19] R. Vincent, P.A. Midgley, Ultramicroscopy 53 (1994) 271.
[20] J.C.H. Spence, J. Taftø, J. Microscopy 130 (1983) 147.
[21] Z. Yu, P.E. Batson, J. Silcox, Ultramicroscopy 96 (2003) 275.
[22] M.F. Murfitt, N. Dellby, O.L. Krivanek, unpublished results.
[23] R.F. Loane, P. Xu, J. Silcox, Acta Cryst. A 47 (1991) 267.
[24] D.A. Muller, et al., Science, 2007, to be published.